

Reverse time migration for microseismic sources using the geometric mean as an imaging condition

Nori Nakata¹ and Gregory C. Beroza¹

ABSTRACT

Time reversal is a powerful tool used to image directly the location and mechanism of passive seismic sources. This technique assumes seismic velocities in the medium and propagates time-reversed observations of ground motion at each receiver location. Assuming an accurate velocity model and adequate array aperture, the waves will focus at the source location. Because we do not know the location and the origin time a priori, we need to scan the entire 4D image (3D in space and 1D in time) to localize the source, which makes time-reversal imaging computationally demanding. We have developed a new approach of time-reversal imaging that reduces the computational cost and the scanning dimensions from 4D to 3D (no time) and increases the spatial resolution of the source image. We first individually extrapolate wavefields at each receiver, and then we crosscorrelate these

wavefields (the product in the frequency domain: geometric mean). This crosscorrelation creates another imaging condition, and focusing of the seismic wavefields occurs at the zero time lag of the correlation provided the velocity model is sufficiently accurate. Due to the analogy to the active-shot reverse time migration (RTM), we refer to this technique as the geometric-mean RTM or GmRTM. In addition to reducing the dimension from 4D to 3D compared with conventional time-reversal imaging, the crosscorrelation effectively suppresses the side lobes and yields a spatially high-resolution image of seismic sources. The GmRTM is robust for random and coherent noise because crosscorrelation enhances signal and suppresses noise. An added benefit is that, in contrast to conventional time-reversal imaging, GmRTM has the potential to be used to retrieve velocity information by analyzing time and/or space lags of crosscorrelation, which is similar to what is done in active-source imaging.

INTRODUCTION

Locations of passive seismic sources caused by fluid injection during fracturing and production provide important information on deformation, fluid movement, and the geomechanical condition of hydrocarbon and geothermal reservoirs (Baig and Urbancic, 2010; Maxwell et al., 2010; Kamei et al., 2015). Source locations are usually determined using a combination of arrival times and ray-based velocity models (Pujol, 2004). Precise relative source locations can be obtained through the use of arrival-time differences between pairs of events (the double-difference technique; Waldhauser and Ellsworth, 2000). To find seismic events from continuous records and estimate accurate arrival times, one can compute the crosscorrelation between known template waveforms and time-windowed continuous data (Shelly et al., 2007a; Zhao et al., 2010). Zhang and Thurber (2003) estimate the event locations and a velocity model using the double-difference technique. With a dense net-

work, we can use the polarities of the first arrivals to estimate the focal mechanism of microseismic events (Eisner et al., 2010).

Improvements in computational power and imaging techniques enable the use of waveforms, rather than simply arrival times, for source location estimation (Kao and Shan, 2004). Based on a wave equation with a given velocity model, we can compute time-reversed extrapolation of the observed wavefields (Fink, 2006). The extrapolated wavefields focus at the location of seismic sources given a reasonably accurate velocity model (Gajewski and Tessmer, 2005). Larmat et al. (2008) estimate the location and the focal mechanism of relatively large glacial earthquakes from time-reversal images. Douma and Snieder (2015) increase the temporal and spatial resolution of images with deconvolution. Because time-reversal imaging uses multiple receivers simultaneously, one can improve the signal-to-noise ratio (S/N) of the image by increasing the number of receivers (Sava, 2011). The extrapolated wavefields

Manuscript received by the Editor 14 May 2015; revised manuscript received 16 November 2015; published online 14 March 2016.

¹Stanford University, Stanford, California, USA. E-mail: nnakata@stanford.edu; beroza@stanford.edu.

© 2016 Society of Exploration Geophysicists. All rights reserved.

have four dimensions (time and space), and we must scan the entire 4D volume to find the location of the sources. Artman et al. (2010) consider the problem of location estimation as a migration problem and use the autocorrelation imaging condition. Under this imaging condition, we can collapse the time axis (Claerbout, 1971), and we need to scan only three dimensions, as for reflection images created by active-source migration. The autocorrelation technique is known to smear the image when the number of receivers is insufficient (Artman et al., 2010).

In this study, we propose an alternative passive-source migration technique in which we collapse the time axis and improve the spatial resolution of the image. Because the new migration is based on multidimensional crosscorrelation or the product of wavefields in the frequency domain and is similar to active-shot reverse time migration (RTM), we call it geometric-mean RTM (GmRTM). We first briefly introduce the time-reversal imaging and autocorrelation-based migration and then develop GmRTM. Then, we use a 2D acoustic numerical experiment to show the effectiveness of GmRTM. With the same 2D example, we test GmRTM under different conditions including velocity model errors, noise, and multiple sources. We find that GmRTM works well, and it improves the spatial resolution of the image and reduces the strength of artifacts.

MIGRATION FOR SOURCE LOCATION ESTIMATION

Mathematical tour

We start with simple forward wave propagation from a seismic source location \mathbf{x}_s to receiver \mathbf{x}_r as follows:

$$D(\mathbf{x}_r, t) = \mathcal{F}^{-1}\{S(\mathbf{x}_s, \omega)G(\mathbf{x}_r, \mathbf{x}_s, \omega)\}, \quad (1)$$

where G and S are the Green's function and the source function, respectively; t and ω indicate time and frequency, respectively; D is the recorded wavefield; and \mathcal{F}^{-1} is the inverse Fourier transform.

For time-reversal imaging, we propagate the recorded wavefields in reverse time and obtain the 4D image I as follows:

$$I(\mathbf{x}, t) = \mathcal{F}^{-1}\left\{\sum_i D(\mathbf{x}_{r_i}, \omega) \mathcal{G}^*(\mathbf{x}_{r_i}, \mathbf{x}, \omega)\right\}, \quad (2)$$

where $*$ is the complex conjugate and \mathcal{G} is the approximated Green's function based on a given velocity model (Sava, 2011). The term inside the curly bracket indicates the wavefield extrapolation of the observed data. We can approximate the Green's function using a finite-difference or other numerical solution of the wave equation. We usually back propagate observed records at all receivers simultaneously, and thus the summation in equation 2 is computed implicitly. Because we use the entire observed wavefields $D(\mathbf{x}, \omega)$, time-reversal imaging does not require arrival-time picking; however, we need to find the time t_0 when I shows the maximum amplitude or a reasonably focused image for the seismic events in the 4D cube (Fish, 2012). Therefore, we can use time-reversal imaging for low-S/N data such as microseismic records, in which we cannot accurately pick the arrival times of waves in the data domain.

When we treat each receiver independently, we can crosscorrelate the two receiver wavefields and obtain another imaging condition such as

$$\mathcal{I}_{ij}(\mathbf{x}, 2\tau) = \sum_t W_{r_i}(\mathbf{x}, t - \tau) W_{r_j}(\mathbf{x}, t + \tau), \quad (3)$$

where

$$W_{r_i}(\mathbf{x}, t) = \mathcal{F}^{-1}\{D(\mathbf{x}_{r_i}, \omega) \mathcal{G}^*(\mathbf{x}_{r_i}, \mathbf{x}, \omega)\}. \quad (4)$$

Because wavefields $D(\mathbf{x}_{r_i})$ and $D(\mathbf{x}_{r_j})$ are generated by the same seismic source, wavefields W_{r_i} and W_{r_j} pass the source location at the same time; therefore, we need to consider only $\tau = 0$ when \mathcal{G} is accurate (Claerbout, 1971). Images constructed by different receiver pairs provide the same source image with different artifacts, and hence the average of all receiver pairs should enhance the amplitude of the source image and suppress artifacts:

$$\begin{aligned} \mathcal{I}(\mathbf{x}) &= \sum_i \sum_j \mathcal{I}_{ij}(\mathbf{x}) \\ &= \sum_t \left\{ \sum_i W_{r_i}(\mathbf{x}, t) \right\} \left\{ \sum_j W_{r_j}(\mathbf{x}, t) \right\} \\ &= \sum_t I(\mathbf{x}, t) I(\mathbf{x}, t). \end{aligned} \quad (5)$$

Equation 5 is equivalent to the autocorrelation of time-reversal images at zero time lag, and it is the same as equation 2 in Artman et al. (2010). Note that because of the correlation, we collapse the time axis in the image in equation 5.

For a zero time lag, $\mathcal{I}_{ij}(\mathbf{x})$ (equation 3) is a product of two receiver wavefields. Rather than summing over all images (equation 5), we can multiply all receiver wavefields as an extension of equation 3 to obtain a new imaging condition as follows:

$$\mathfrak{I}(\mathbf{x}) = \sum_t \prod_i W_{r_i}(\mathbf{x}, t). \quad (6)$$

We refer to this as GmRTM because the product plays the same role for the geometric mean as the same for the arithmetic mean and due to the analogy to the active-shot RTM as explained in the next subsection. We can interpret this product as a multidimensional cross-correlation (Arfken et al. [2013], p. 990) and still collapse the time axis. In GmRTM, we first extrapolate wavefields at each receiver (i.e., compute $W_{r_i}(\mathbf{x}, t)$). Then, when we consider only the zero time lag, we multiply all receiver wavefields at each space and time sample, and then we sum them over the time axis. We can compute the multiplication in the frequency domain as well. For the two-receiver case, equation 6 is equivalent to equation 3. Compared with equation 6, equation 2 ($I(\mathbf{x}, t) = \sum_i W_{r_i}(\mathbf{x}, t)$) can be considered the arithmetic-mean RTM (AmRTM).

GmRTM requires solving the wave equation independently for each receiver, which can be computationally demanding. To reduce the computational cost for wavefield extrapolation, we can group several receivers and solve the extrapolation problem for each group (J. Sun and S. Fomel, personal communication, 2015); however, this comes at a cost of reduced image resolution, and the choice of the set of receivers for each group is not trivial.

Importantly, GmRTM does not require computing Green's functions (calculating finite difference solutions of wave equations) for each time interval. Instead, we can use the same Green's function

at each receiver for different time intervals because the relationship between the Green's function and the records is linear (equation 2). The length of the records (days to years) is much longer than the length of the Green's function that we are interested in to represent the wave propagation from the source to the receivers (seconds to tens of seconds). Therefore, we first solve the wave equation for each receiver (i.e., estimate $\mathcal{G}^*(\mathbf{x}_{r_i}, \mathbf{x}, \omega)$ for each r_i) and we convolve with the observed data ($D(\mathbf{x}_{r_i}, \omega)$) in the image domain. For AmRTM, however, when we solve equation 2 for all receivers simultaneously, we need to solve it for each time interval because the summation over the receivers breaks the linearity. This indicates that GmRTM has a much lower computational cost for carrying out the finite-difference operation than does AmRTM for continuous data.

For example, when we continuously record ground motion for 50 days with 1000 receivers, if we are interested in microseismic sources located within 30 s from the receivers, we need to compute the Green's function for 30 s. The total numerical time of the finite difference is $1000 \times 30 = 30,000$ s for GmRTM and $1 \times 50 \times 24 \times 60 \times 60 = 4,320,000$ s for AmRTM. Therefore, the computational cost for GmRTM is more than 100 times less than for conventional back projection. Here, we assume that we cannot find the events' waveforms in the data domain (low S/N data). Two notes should be made here: First, if we compute the Green's function for each receiver, convolve with data, and then average over all receivers, the computational cost of AmRTM becomes almost equal to that of GmRTM. Second, when we can find the events' waveforms in the data domain (high S/N data) and we only need to image these events, AmRTM requires a lower computational cost than does GmRTM. Hence, AmRTM is suitable for data sets that have many receivers and short recording times when we do not consider the resolution or other benefits of GmRTM discussed below.

Moreover, finding source locations from 4D images given by AmRTM can be difficult because images may not have a clear, isolated maximum as shown below with the numerical examples. Sharpening the image and reducing the search dimension provide an important advantage. In particular, searching for imaged events through time in AmRTM can be very time consuming and requires subjective interpretation.

Analogy to active-shot RTM based on seismic interferometry

We can interpret equation 3 as an active-shot RTM (Baysal et al., 1983) in which we consider one receiver as a virtual source within the concept of convolution-based seismic interferometry (Schuster, 2009). Figure 1a shows the wave propagation generated by a seismic source at \mathbf{x}_s . We represent the data related to this source in equation 1. For simplicity, we assume that the source function is a delta function in the time domain, such that the convolution function between the observed data at receivers r_i and r_j is $G(\mathbf{x}_{r_i}, \mathbf{x}_s)G(\mathbf{x}_{r_j}, \mathbf{x}_s)$ in the frequency domain. This convolution function is similar to the virtual-reflector signals after an appropriate integral over sources (Poletto and Farina, 2010). Because we are interested in seismic sources distributed discretely in space (i.e., no integral is computed), we can consider the sources as virtual scatterers and the receiver r_i as a virtual source as shown in

Figure 1b (with reciprocity $G(\mathbf{x}_{r_i}, \mathbf{x}_s) = G(\mathbf{x}_s, \mathbf{x}_{r_i})$). Applying an active-shot RTM to the convolution function, we obtain an image of the virtual scatterer (i.e., seismic source) as follows:

$$\mathbf{i}(\mathbf{x}) = \sum_{\omega} \mathcal{G}^*(\mathbf{x}, \mathbf{x}_{r_i}) [G(\mathbf{x}_{r_i}, \mathbf{x}_s)G(\mathbf{x}_{r_j}, \mathbf{x}_s)\mathcal{G}^*(\mathbf{x}, \mathbf{x}_{r_j})], \quad (7)$$

where the first term on the right side represents the virtual-source wavefields and the bracketed term represents the receiver wavefields (Figure 1c). The complex conjugate on the virtual-source wavefields ($\mathcal{G}^*(\mathbf{x}, \mathbf{x}_{r_i})$) is related to the fact that the imaging condition is given by crosscorrelation. Indeed, equation 7 is equivalent to equation 3 with reciprocity because

$$\begin{aligned} \mathbf{i}(\mathbf{x}) &= \sum_{\omega} [G(\mathbf{x}_{r_i}, \mathbf{x}_s)\mathcal{G}^*(\mathbf{x}_{r_i}, \mathbf{x})][G(\mathbf{x}_{r_j}, \mathbf{x}_s)\mathcal{G}^*(\mathbf{x}_{r_j}, \mathbf{x})] \\ &= \sum_{\omega} W_{r_i}(\mathbf{x})W_{r_j}(\mathbf{x}) = \mathcal{I}_{ij}(\mathbf{x}), \end{aligned} \quad (8)$$

and therefore we use RTM in the name of the proposed technique. For the same reason, we consider equation 5 as autocorrelation RTM. Equation 8 implies that we can use the techniques that were developed in active-source RTM, such as angle-domain gathers (Rickett and Sava, 2002; Sava and Fomel, 2003), migration velocity analysis (Sava and Biondi, 2004a, 2004b), and extended imaging condition (Sava and Vasconcelos, 2011) to GmRTM. In addition, due to this similarity, GmRTM can be applied for diffraction imaging (Khaidukov et al., 2004) as well.

Numerical tests

We use 2D acoustic finite-difference numerical modeling (Nakata et al., 2011) to illustrate the benefits of GmRTM. Although we use only a 2D acoustic medium, we can apply GmRTM to 3D and elastic cases as well. For 3D, the concept of RTM is the same as that for 2D, but the computational cost is increased. For the elastic case, we can, e.g., use Helmholtz decomposition to scalarize the wavefields before RTM (Yan and Sava, 2008; Artman et al., 2010; Duan and Sava, 2014). We use a part of the Marmousi model to introduce some complexity into the numerical experiments (Figure 2a). The part of the model we use is 4.5–7.5 km in the horizontal axis and 0.55–1.55 km in the vertical axis of the P velocities of the Marmousi2 model. We do not include the free surface in the model. We introduce a seismic source, which we show with a blue cross in Figure 2a located just below the high-velocity layer ($(x, z) = (1.5, 0.7)$ km) and four receivers that record seismic

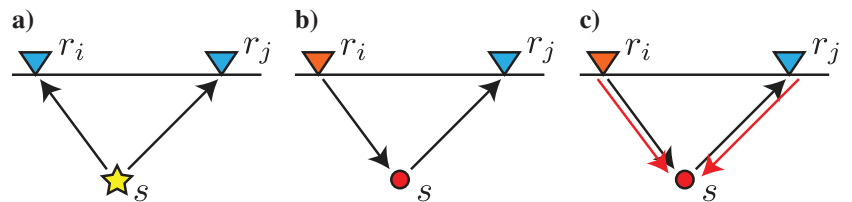


Figure 1. Schematic cartoons of (a) observation, (b) virtual active shot, and (c) reverse time migration of the virtual active shot. The black arrows show the direction of forward wave propagation, and the red arrows are wave propagation for imaging.

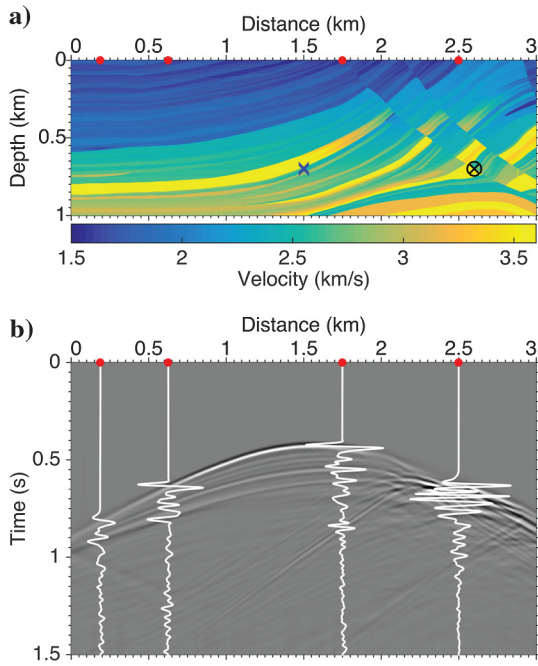


Figure 2. (a) Acoustic velocity model (a part of the Marmousi model). The blue \times and the red dots indicate the locations of the source and receivers, respectively. The black \otimes at (2.6, 0.7) km shows another source location used in Figure 6. (b) Recorded data. The background image is the wavefields at the surface, and the white lines illustrate the waveforms observed at each receiver.

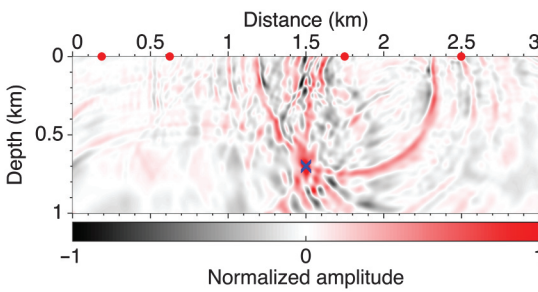


Figure 3. Time reversal image (equation 2, $I(\mathbf{x}, t_0)$) using the correct velocity for migration. The blue \times and the red dots show the locations of the source and receivers, respectively.

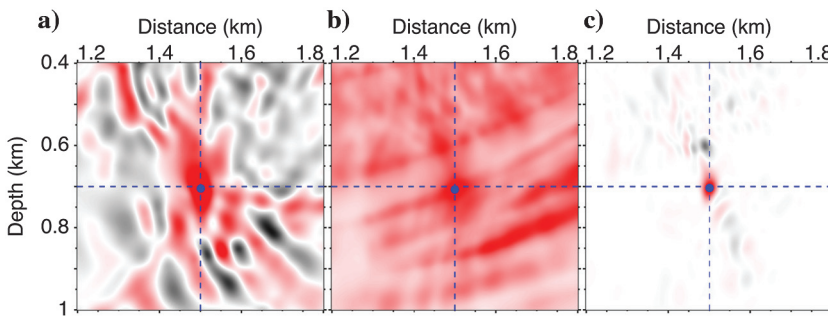


Figure 4. Images around the source location obtained by (a) AmRTM (equation 2, $I(\mathbf{x}, t_0)$), (b) autocorrelation RTM (equation 5, $\mathcal{I}(\mathbf{x})$), and (c) GmRTM (equation 6, $\mathfrak{I}(\mathbf{x})$). The amplitudes are independently normalized at each panel. The blue dashed lines show the depth and horizontal locations of the source. The blue dot indicates the location of the maximum amplitude for each image.

waves at the surface (the red dots in Figure 2a). The source function is a Ricker wavelet (peak frequency of 30 Hz). For the wavefield modeling, the time and space sampling intervals are 0.15 ms and 1.249 m, respectively. Here, we use the correct velocity model for migration, and we defer the discussion of the influence of velocity model errors.

The time-reversal imaging (AmRTM, equation 2) at time t_0 of the maximum amplitude of $I(\mathbf{x}, t)$ provides the image of the source location (Figure 3). Because we use the correct velocity model for migration and the Ricker wavelet as a source function, the time t_0 shows the origin time of the source. Although strong artifacts are present due to the small number of receivers, the waves are correctly focused at the true location of the source (Figure 4a). The autocorrelation RTM (equation 5) provides an image without the time axis, but the image is strongly smeared due to the small number of receivers and the complex velocity model (Figure 4b). The amplitudes of the image are all positive due to the autocorrelation. The GmRTM (equation 6) creates the clearest source image and suffers fewer artifacts (Figure 4c). Note that GmRTM also collapses the time axis, and thus we need to scan only the space axes to find the source location.

For autocorrelation RTM and GmRTM, we average over the entire time interval to create the images in Figure 4. We can choose an arbitrary time interval for averaging if we know the onset time of seismic sources (e.g., a perforation shot) or we are interested in the time sequence of sources. Therefore, GmRTM can handle multiple sources emitted at different times and can have the same temporal resolution as AmRTM, but averaging over the entire time interval reduces the cost of the searching process, which is nontrivial.

Figure 5 shows the vertical and horizontal traces of each image. The GmRTM results in the sharpest image, especially in the depth direction, which is attributable to the multiplication of Ricker wavelets resulting in a sharper wavelet in the time domain. We discuss the ability of GmRTM to create images with high spatial resolution and to separate two nearby sources due to this multiplication in the next section. Importantly, GmRTM shows almost zero amplitude away from the source location (few artifacts), and hence we are less likely to misinterpret imaging artifacts as seismic sources using GmRTM. In any RTMs based on surface recordings, the image smears more vertically because the receivers are distributed horizontally resulting in increased crossrange resolution (Borcea et al., 2003).

We also test GmRTM to put a source at a geologically more challenging location for imaging (the black \otimes in Figure 2). All receivers are on the left side of the source, and the geology in the vicinity is complex. Although both images are degraded compared with the image of the source that is recorded by the wide-aperture array (Figure 4), GmRTM constructs the image with fewer artifacts than does AmRTM (Figure 6). The GmRTM image smears into the top-left side of the source location. This image portion is caused by strong waves that are guided by the low-velocity zone. The AmRTM images are not smeared by these guided waves because the image in Figure 6 is a time slice. It is likely that this would have been interpreted as another source if searching for sources at different times via AmRTM processing.

DISCUSSION

Here, we address the effects of velocity model errors, finite-time source wavelets, and random/coherent noise on GmRTM and the improvement in spatial resolution that results from the multiplication of many waveforms and how it improves the ability to discern clear images of multiple sources. All of these factors are important to consider for applications with real data. For all examples, we use the same parameters as the previous numerical test, unless noted.

Velocity model error

First, we use a smoothed velocity model (smoothed with a $100 \times 100 \text{ m}^2$ 2D triangular filter [Claerbout, 2014], not shown) for migration, which is more reasonable than using the correct velocity model due to the limitations in velocity estimation. Because the mean velocity along the raypaths is nearly correct, the wavefields are still focused around the correct source location with either AmRTM or GmRTM (Figure 7a), but the images are smeared compared with Figure 4. The maximum amplitudes of the images decrease approximately 50%. GmRTM works better in this case based on the better localization of maximum amplitude and lesser degree of smearing.

Another realistic case is when mean velocities differ from the correct velocities. To test the effect of such errors, we introduce 5% and 10% velocity errors for migration velocities (Figure 7b and 7c). Because the migration velocities are slower than the true velocities, the image of the seismic sources shift deeper, and the errors degrade the images for both RTM results. Based on the amplitudes of the images, GmRTM is clearly sensitive to the velocity model, and we obtain an amplitude as low as 20% from the im-

perfect focusing of wavefields in Figure 7c compared with the image in Figure 4c. AmRTM is less sensitive to the velocity model; however, that also means it has a larger chance of focusing at an incorrect location. As with the active-shot RTM (Sava and Vasconcelos, 2011) because we have time and space lags in the image (equation 3), we can still detect the seismic sources and update the velocity model with GmRTM even when starting migration velocities are not accurate. Inversion techniques for migration velocity analysis are beyond the scope of this study.

Length of source wavelet and noise

Averaging over time in GmRTM (equation 6) reduces the computational effort required for source imaging; moreover, it will also increase the S/N of the image when seismic events have finite-length source durations. The rupture process of some seismic events takes seconds to a few minutes (Shelly et al., 2007b; Suzuki et al., 2011). Figure 8a shows synthetic records computed with a 0.225 s wavelet. The wavelet contains energies between 5 and 40 Hz. After migrating these records, GmRTM produces a sharp image of the seismic source (Figure 9a). The sharpness of the image at the source location is not very different from Figure 4c. At approximately 50 and 100 m below the correct source location, GmRTM creates two more bright spots, although the amplitudes are reduced by approximately 50% from the maximum amplitude in the image. These images may be the result of the interference of direct and reflected waves because all RTMs used in this study are based on the Born approximation. Because we choose t_0 when the image has the largest amplitude, AmRTM does not focus at the correct source location and has multiple broad, large-amplitude spots (Figure 9a). Because the image of AmRTM is a time slice, AmRTM cannot use the majority of energy generated by the source for imaging when the source wavelet/duration is extended in time.

When we add two types of noise (random and coherent) to the synthetic records (Figure 8b), the images are further degraded (Figure 9b). The random noise is a band-limited white noise (5–40 Hz), and the amplitude of the random noise is 50% of the maximum amplitude of noise-free data shown in Figure 8a. For the coherent noise, we inject additional band-limited white noise (5–40 Hz with 10% amplitude) at $(x, z) = (1.5, 0.02)$ km. This coherent noise might represent persistent sources of cultural interference such as can arise from pumping or traffic. After adding the noise, finding the seismic signature of the event in the data (the white lines in Figure 8a) is essentially impossible; however, Figure 9b shows that GmRTM still provides an amplitude peak around the source location (more than twice the amplitude of other maxima in the image). Here again, the crosscorrelation and time averaging (equation 6)

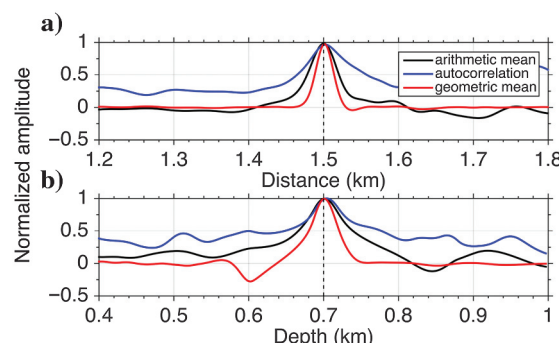


Figure 5. Amplitudes of the images shown in Figure 4 at (a) fixed depth and at (b) fixed distance of the source (the blue dashed lines in Figure 4). The black dashed lines indicate the location of the source.

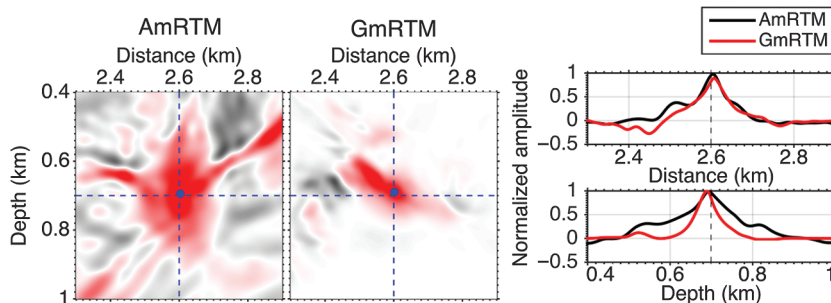


Figure 6. Images obtained from the data generated by the source at the black \otimes in Figure 2. The blue dots show the location of the maximum amplitude of each image. The amplitudes are independently normalized at each panel. The right column shows the amplitudes of the images at fixed depth (top) and at a fixed distance (bottom) from the source.

help to suppress the noise in the image. However, AmRTM does not focus the wavefields.

The viability of traveltime picking to detect seismic sources depends on discerning discrete arrivals at each receiver. When seismic events are strong and data have high S/N, we can accurately estimate the arrival times of waves; however, finding the arrival times for small earthquakes is more challenging. To increase the detectability of smaller events, we should use more information in the time and/or space domains. For example, template-matching and

autocorrelation techniques use finite time samples (Shelly et al., 2007a). Time-reversal methods take advantage of using multiple receivers simultaneously (Xuan and Sava, 2010). Depending on imaging conditions, migration-based approaches also use multiply scattered waves for detection (Fleury and Vasconcelos, 2012). The GmRTM can use the finite time samples and multiple receivers to find seismic events (equation 6); therefore, GmRTM can be expected to have higher detectability than the techniques using only space or time samples. In other words, GmRTM effectively uses

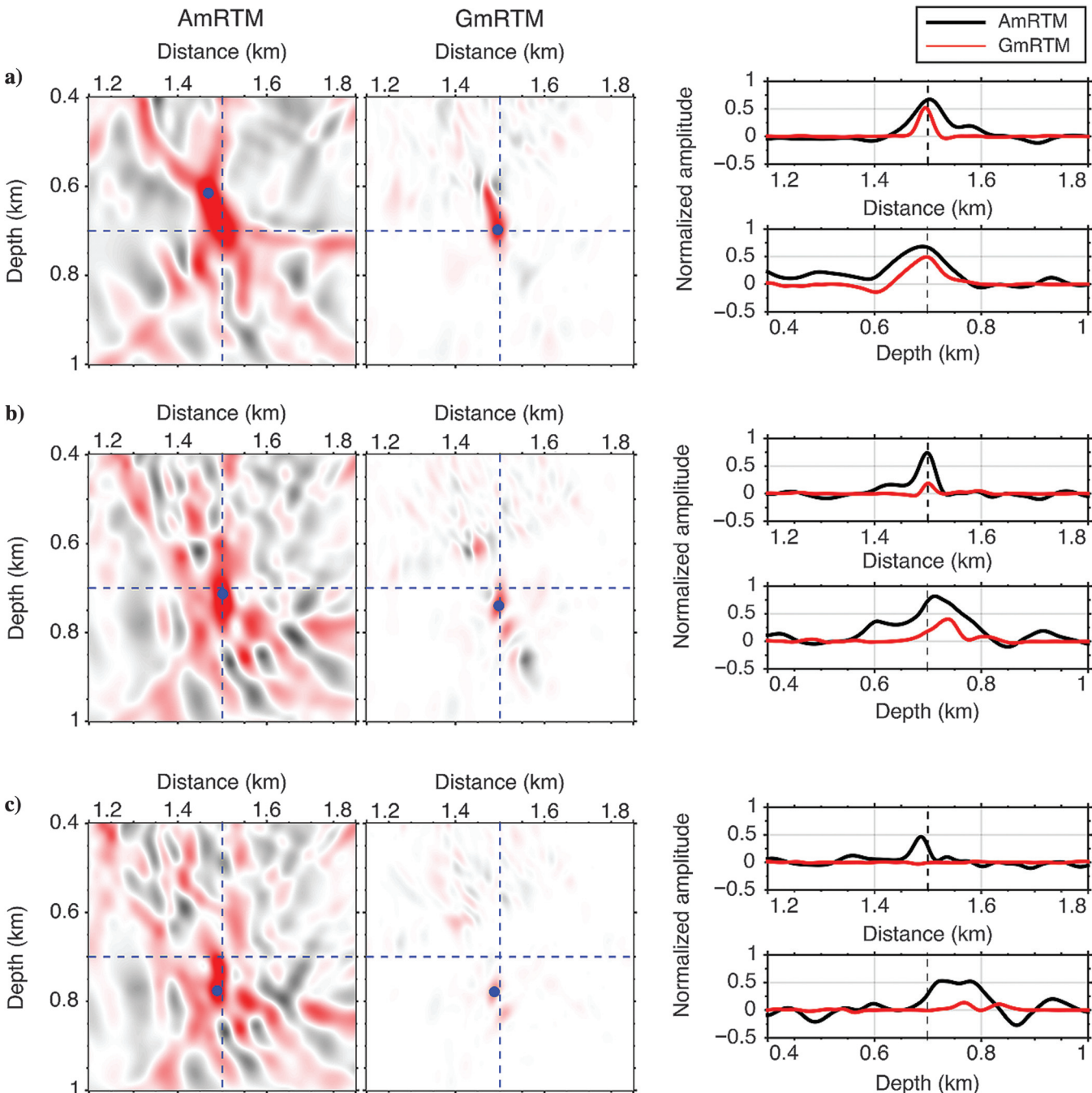


Figure 7. Images developed in the presence of velocity errors: using (a) smoothed velocity model, (b) 5% slow velocity, and (c) 10% slow velocity. The blue dots show the location of the maximum amplitude of each image. Amplitudes are normalized as in Figure 4. The right column shows the amplitudes of the images at fixed depth (top) and at fixed distance (the source).

signals scattered in time and space (Figure 8) to construct a source image. Increasing the detectability is important because smaller events are linked to larger events (Gutenberg and Richter, 1956).

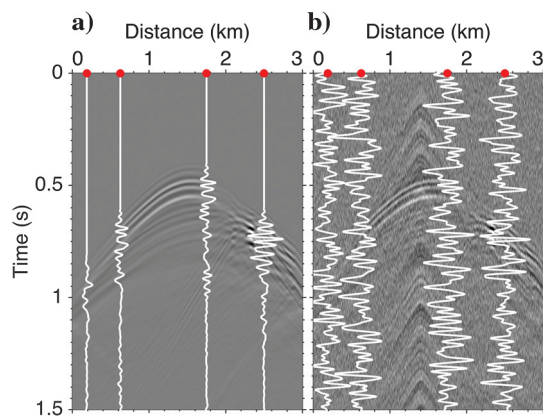


Figure 8. (a) Similar to Figure 2b but for a source wavelet of 0.225 s duration. (b) Same as panel (a) but with band-limited random noise and coherent noise added.

Spatial resolution

We also test the ability of GmRTM to image multiple sources. During hydraulic fracturing, earthquake swarms, or tremor, many sources will occur in close temporal and spatial proximity (Shelly et al., 2007a; Maxwell et al., 2010; Hauksson et al., 2013). For this example, we place an additional source 48 m below the one we used previously (Figure 10a). These sources act at the same time with the same amplitude and frequency range. Because the velocity at the source locations is approximately 2.5 km/s, the source separation of 48 m is about a half wavelength. Also, because the image tends to smear vertically, two sources that are vertically aligned will be challenging to image. The image created by GmRTM clearly separates two sources better than AmRTM does (Figure 10a). In addition, as we observe in other examples, GmRTM has fewer artifacts in the image. These trends are more obvious when we use eight receivers (Figure 10b). We place an additional four receivers at the center of each receiver pair in Figure 2 (two receivers are added between the second and third receivers). This improves both images. The wavefields are slightly improved in AmRTM, but the GmRTM image is exceptionally clear, with just two bright spots at the correct source locations. The width of the images is much smaller than the wave-

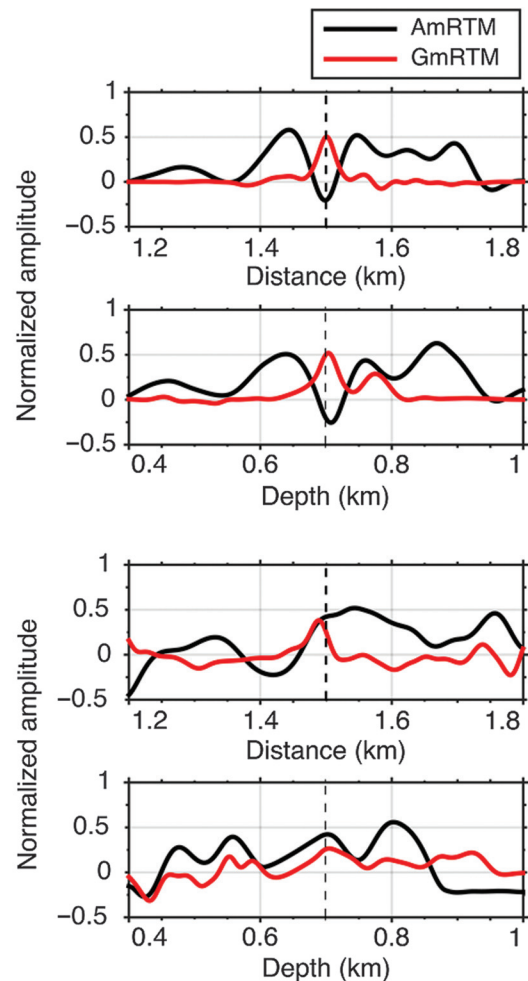
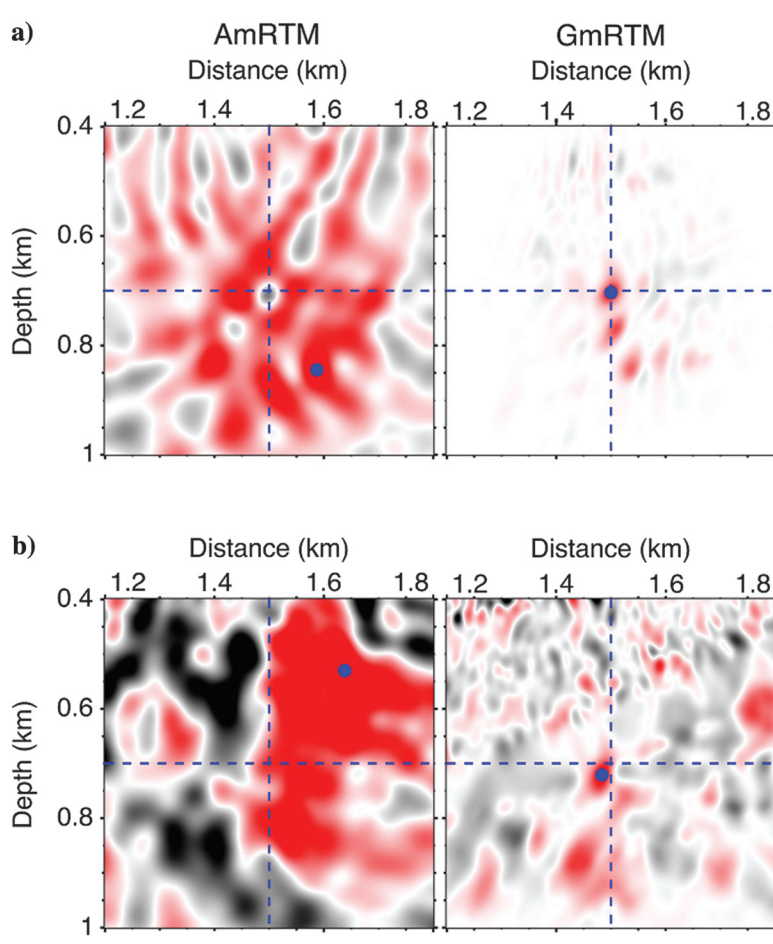


Figure 9. Images reconstructed from the data shown in Figure 8. Panels (a and b) correspond to the data in Figure 8a and 8b, respectively. The right column shows the amplitudes of the images at fixed depth (top) and at fixed distance (bottom) of the source.

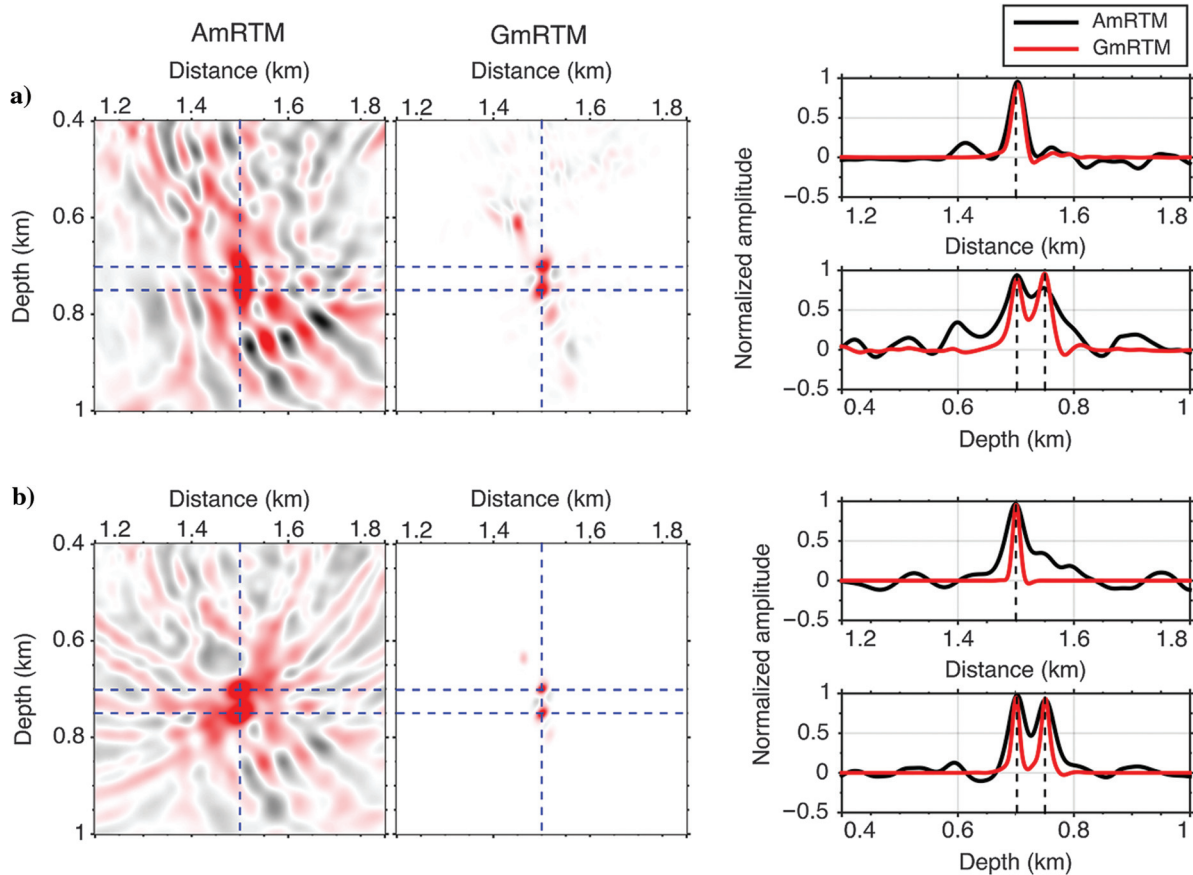


Figure 10. (a) Image obtained for two simultaneously excited sources. The locations of two sources are illustrated by the intersections of the dashed lines in the images. The depth of the horizontal slice of the image is that of the shallower source. (b) Same as panel (a), but we use eight receivers instead of four. The right column shows the amplitudes of the images at fixed depth (top) and at fixed distance (bottom) of the shallower source.

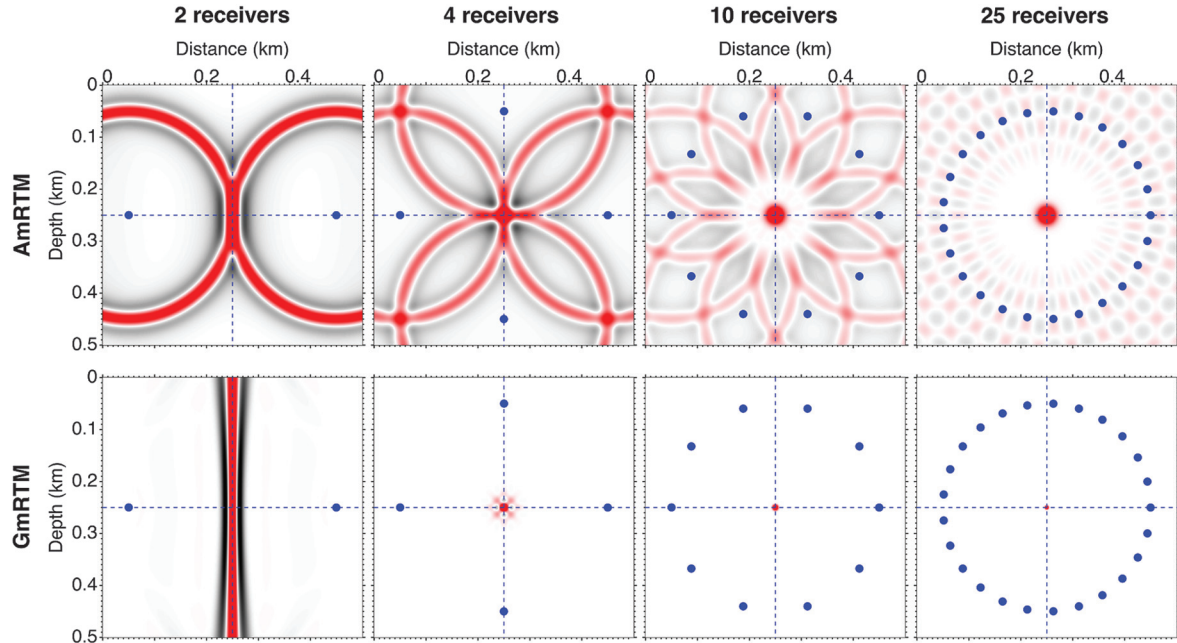


Figure 11. Source images obtained by AmRTM and GmRTM with different number of receivers. The model is an acoustic homogeneous model with velocity of 2 km/s, and the source is located at the center of the model (the intersection of blue dashed lines). The source function is the Ricker wavelet with 40 Hz peak frequency. The blue dots show the locations of receivers used for each image. For AmRTM, we use the correct source-excitation time for each image.

length, which indicates that the GmRTM has the potential to image with superresolution (Park et al., 2003). We can also use deconvolution instead of crosscorrelation for the imaging condition in equation 6 to increase the spatial and temporal resolution (Chattopadhyay and McMechan, 2008).

A homogeneous-model example shows that GmRTM surpasses the diffraction limit of time-reversal imaging (Figure 11). Because we use a band-limited impulsive source for this numerical test, one can consider that the images are the array response. When we increase the number of receivers used, we obtain better S/N images for AmRTM and GmRTM. For AmRTM, diffraction limits blur the source images and the size of imaged sources does not change from 10 to 25 receivers. When the number of receivers increases, the image of GmRTM better focuses on the source location even from 10 to 25 receivers. Obviously, the focusing size of GmRTM is much smaller than AmRTM.

CONCLUSIONS

We develop GmRTM for estimation of the passive seismic source location. GmRTM is a correlation-based imaging technique, and to find the source location, we need to scan only the space axes, not the time axis. The computational cost of GmRTM for continuous records is much smaller than for conventional back-projection techniques. Compared with time-reversal imaging (AmRTM) or autocorrelation RTM, GmRTM creates spatially higher resolution source images. Although GmRTM is sensitive to the velocity model (at least as sensitive as AmRTM), we can use time/space lags of crosscorrelation to update the velocity model. GmRTM is robust with respect to the random and coherent noise because the cross-correlation effectively suppresses noise in both cases. It is better suited to imaging sources extended in time than AmRTM is due to the collapse of the time axis. The increase in the spatial resolution of images in GmRTM provides a greater ability to separate multiple sources excited close to each other in space and time. Similar to other imaging techniques, GmRTM is scale independent, and thus we can apply it from the microseismic to crustal scales. Application to the 3D data sets is a simple extension, but extension to the elastic case remains a future research topic. Migration velocity analyses using GmRTM for microseismic sources will also be an interesting future research direction.

ACKNOWLEDGMENTS

We are grateful to the Center for Computational Earth and Environmental Science, the Stanford Research Computing Center, and SuperMicro Computer Inc. for providing computer resources. We thank the editor, associate editor, and three anonymous reviewers for their comments. N. Nakata appreciates the financial support of the George Thompson Postdoctoral Fellowship from the Department of Geophysics, Stanford University.

REFERENCES

- Arfken, G. B., H. J. Weber, and F. E. Harris, 2013, Mathematical methods for physicists, 7th ed.: Elsevier.
- Artman, B., I. Podladchikov, and B. Witten, 2010, Source location using time-reverse imaging: *Geophysical Prospecting*, **58**, 861–873, doi: [10.1111/j.1365-2478.2010.00911.x](https://doi.org/10.1111/j.1365-2478.2010.00911.x).
- Baig, A., and T. Urbancic, 2010, Microseismic moment tensors: A path to understanding frag growth: *The Leading Edge*, **29**, 320–324, doi: [10.1190/1.3353729](https://doi.org/10.1190/1.3353729).
- Baysal, E., D. D. Kosloff, and J. W. C. Sherwood, 1983, Reverse time migration: *Geophysics*, **48**, 1514–1524, doi: [10.1190/1.1441434](https://doi.org/10.1190/1.1441434).
- Borcea, L., G. Papanicolaou, and C. Tsogka, 2003, Theory and applications of time reversal and interferometric imaging: *Inverse Problems*, **19**, S139–S164, doi: [10.1088/0266-5611/19/6/058](https://doi.org/10.1088/0266-5611/19/6/058).
- Chattopadhyay, S., and G. A. McMechan, 2008, Imaging conditions for pre-stack reverse-time migration: *Geophysics*, **73**, no. 3, S81–S89, doi: [10.1190/1.2903822](https://doi.org/10.1190/1.2903822).
- Claerbout, J., 2014, Geophysical image estimation by example: lulu.com.
- Claerbout, J. F., 1971, Toward a unified theory of reflector mapping: *Geophysics*, **36**, 467–481, doi: [10.1190/1.1440185](https://doi.org/10.1190/1.1440185).
- Douma, J., and R. Snieder, 2015, Focusing of elastic waves for microseismic imaging: *Geophysical Journal International*, **200**, 390–401, doi: [10.1093/gji/gju398](https://doi.org/10.1093/gji/gju398).
- Duan, Y., and P. Sava, 2014, Imaging condition for elastic RTM: CWP Research Reports.
- Eisner, L., S. Williams-Stroud, A. Hill, P. Duncan, and M. Thornton, 2010, Beyond the dots in the box: microseismicity-constrained fracture models for reservoir simulation: *The Leading Edge*, **29**, 326–333, doi: [10.1190/1.3353730](https://doi.org/10.1190/1.3353730).
- Fink, M., 2006, Time-reversal acoustics in complex environments: *Geophysics*, **71**, no. 4, S1151–S1164, doi: [10.1190/1.2215356](https://doi.org/10.1190/1.2215356).
- Fish, A. M., 2012, Microseismic velocity inversion and event location using reverse time imaging: Master's thesis, Colorado School of Mines.
- Fleury, C., and I. Vasconcelos, 2012, Imaging condition for nonlinear scattering-based imaging: Estimate of power loss in scattering: *Geophysics*, **77**, no. 1, S1–S18, doi: [10.1190/geo2011-0135.1](https://doi.org/10.1190/geo2011-0135.1).
- Gajewski, D., and E. Tessmer, 2005, Reverse modelling for seismic event characterization: *Geophysical Journal International*, **163**, 276–284, doi: [10.1111/j.1365-246X.2005.02732.x](https://doi.org/10.1111/j.1365-246X.2005.02732.x).
- Gutenberg, B., and C. F. Richter, 1956, Magnitude and energy of earthquakes: *Annals of Geophysics*, **9**, 1–15.
- Hauksson, E., J. Stock, R. Bilham, M. Boese, X. Chen, E. J. Fielding, J. Galetzka, K. W. Hudnut, K. Hutton, L. M. Jones, H. Kanamori, P. M. Shearer, J. Steidl, J. Treiman, S. Wei, and W. Yang, 2013, Report on the August 2012 Brawley earthquake swarm in Imperial Valley, Southern California: *Seismological Research Letters*, **84**, 177–189, doi: [10.1785/0220120169](https://doi.org/10.1785/0220120169).
- Kamei, R., N. Nakata, and D. Lumley, 2015, Introduction to microseismic source mechanisms: *The Leading Edge*, **34**, 876–880, doi: [10.1190/tle34080876.1](https://doi.org/10.1190/tle34080876.1).
- Kao, H., and S.-J. Shan, 2004, The source-scanning algorithm: Mapping the distribution of seismic sources in time and space: *Geophysical Journal International*, **157**, 589–594, doi: [10.1111/j.1365-246X.2004.02276.x](https://doi.org/10.1111/j.1365-246X.2004.02276.x).
- Khaidukov, V., E. Landa, and T. J. Moser, 2004, Diffraction imaging by focusing-defocusing: An outlook on seismic superresolution: *Geophysics*, **69**, 1478–1490, doi: [10.1190/1.1836821](https://doi.org/10.1190/1.1836821).
- Larmat, C., J. Tromp, Q. Liu, and J.-P. Montagner, 2008, Time reversal location of glacial earthquakes: *Journal of Geophysical Research*, **113**, B09314.
- Maxwell, S. C., J. Rutledge, R. Jones, and M. Fehler, 2010, Petroleum reservoir characterization using downhole microseismic monitoring: *Geophysics*, **75**, no. 5, 75A129–75A137, doi: [10.1190/1.3477966](https://doi.org/10.1190/1.3477966).
- Nakata, N., T. Tsuji, and T. Matsuoka, 2011, Acceleration of computation speed for elastic wave simulation using graphic processing unit: *Exploration Geophysics*, **42**, 98–104, doi: [10.1071/EG10039](https://doi.org/10.1071/EG10039).
- Park, S. C., M. K. Park, and M. G. Kang, 2003, Super-resolution image reconstructions: A technical overview: *IEEE Signal processing magazine*, **20**, 21–36.
- Poletto, F., and B. Farina, 2010, Synthesis and composition of virtual-reflector (VR) signals: *Geophysics*, **75**, no. 4, SA45–SA59, doi: [10.1190/1.3433311](https://doi.org/10.1190/1.3433311).
- Pujol, J., 2004, Earthquake location tutorial: Graphical approach and approximate epicentral location techniques: *Seismological Research Letters*, **75**, 63–74, doi: [10.1785/gssrl.75.1.63](https://doi.org/10.1785/gssrl.75.1.63).
- Rickett, J. E., and P. C. Sava, 2002, Offset and angle-domain common image-point gathers for shot-profile migration: *Geophysics*, **67**, 883–889, doi: [10.1190/1.1484531](https://doi.org/10.1190/1.1484531).
- Sava, P., 2011, Micro-earthquake monitoring with sparsely sampled data: *Journal of Petroleum Exploration and Production Technology*, **1**, 43–49, doi: [10.1007/s13202-011-0005-7](https://doi.org/10.1007/s13202-011-0005-7).
- Sava, P., and B. Biondi, 2004a, Wave-equation migration velocity analysis. II. Subsalt imaging examples: *Geophysical Prospecting*, **52**, 607–623, doi: [10.1111/j.1365-2478.2004.00448.x](https://doi.org/10.1111/j.1365-2478.2004.00448.x).
- Sava, P., and B. Biondi, 2004b, Wave-equation migration velocity analysis. I. Theory: *Geophysical Prospecting*, **52**, 593–606, doi: [10.1111/j.1365-2478.2004.00447.x](https://doi.org/10.1111/j.1365-2478.2004.00447.x).
- Sava, P. C., and S. Fomel, 2003, Angle-domain common-image gathers by wavefield continuation methods: *Geophysics*, **68**, 1065–1074, doi: [10.1190/1.1581078](https://doi.org/10.1190/1.1581078).
- Sava, P., and I. Vasconcelos, 2011, Extended imaging conditions for wave-equation migration: *Geophysical Prospecting*, **59**, 35–55, doi: [10.1111/j.1365-2478.2010.00888.x](https://doi.org/10.1111/j.1365-2478.2010.00888.x).
- Schuster, G., 2009, Seismic interferometry: Cambridge University Press.

- Shelly, D. R., G. C. Beroza, and S. Ide, 2007a, Complex evolution of transient slip derived from precise tremor locations in western Shikoku, Japan: *Geochemistry Geophysics Geosystems*, **8**, Q10014.
- Shelly, D. R., G. C. Beroza, and S. Ide, 2007b, Non-volcanic tremor and low-frequency earthquake swarms: *Nature*, **446**, 305–307, doi: [10.1038/nature05666](https://doi.org/10.1038/nature05666).
- Suzuki, W., S. Aoi, H. Sekiguchi, and T. Kunugi, 2011, Rupture process of the 2011 Tohoku-Oki mega-thrust earthquake (M9.0) inverted from strong-motion data: *Geophysical Research Letters*, **38**, L00G16.
- Waldbauer, F., and W. L. Ellsworth, 2000, A double-difference earthquake location algorithm: Method and application to the Northern Hayward Fault, California: *Bulletin of the Seismological Society of America*, **90**, 1353–1368, doi: [10.1785/0120000006](https://doi.org/10.1785/0120000006).
- Xuan, R., and P. Sava, 2010, Probabilistic microearthquake location for reservoir monitoring: *Geophysics*, **75**, no. 3, MA9–MA26, doi: [10.1190/1.3417757](https://doi.org/10.1190/1.3417757).
- Yan, J., and P. Sava, 2008, Isotropic angle-domain elastic reverse-time migration: *Geophysics*, **73**, no. 6, S229–S239, doi: [10.1190/1.2981241](https://doi.org/10.1190/1.2981241).
- Zhang, H., and C. H. Thurber, 2003, Double-difference tomography: The method and its application to the Hayward Fault, California: *Bulletin of the Seismological Society of America*, **93**, 1875–1889, doi: [10.1785/0120020190](https://doi.org/10.1785/0120020190).
- Zhao, P., Z. Peng, and K. G. Sabra, 2010, Detecting remotely triggered temporal changes around the Parkfield section of the San Andreas fault: *Earthquake Science*, **23**, 497–509, doi: [10.1007/s11589-010-0748-0](https://doi.org/10.1007/s11589-010-0748-0).